

Yb Valence Change in $\text{Ce}_{1-x}\text{Yb}_x\text{CoIn}_5$ from spectroscopy and bulk properties

L. Dudy^{1,4}, J. D. Denlinger², L. Shu^{3,5}, M. Janoschek^{3,6}, J. W. Allen¹, and M.B. Maple³

¹*Randall Laboratory, University of Michigan, Ann Arbor, MI 48109-1040, USA*

²*Advanced Light Source, Lawrence Berkeley National Laboratory, Berkeley, CA, 94720, USA*

³*Department of Physics, University of California, San Diego, La Jolla, CA, 92093, USA*

⁴*Physikalisches Institut, Universität Würzburg, Am Hubland, 97074 Würzburg, Germany*

⁵*State Key Laboratory of Surface Physics, Department of Physics, Fudan University, Shanghai 200433, People's Republic of China*

⁶*Condensed Matter and Magnet Science group, Los Alamos National Laboratory, Los Alamos, New Mexico 87545, USA*

(Dated: March 26, 2013)

The electronic structure of $\text{Ce}_{1-x}\text{Yb}_x\text{CoIn}_5$ has been studied by a combination of photoemission, x-ray absorption and bulk property measurements. Previous findings of a Ce valence near 3+ for all x and of an Yb valence near 2.3+ for $x \geq 0.3$ were confirmed. One new result of this study is that the Yb valence for $x \leq 0.2$ increases rapidly with decreasing x from 2.3 toward 3+, which correlates well with de Haas van Alphen results showing a change of Fermi surface around $x=0.2$. Another new result is the direct observation by angle resolved photoemission Fermi surface maps of $\approx 50\%$ cross sectional area reductions of the α and β sheets for $x = 1$ compared to $x = 0$, and a smaller, essentially proportionate, size change of the α sheet for $x = 0.2$. These changes are found to be in good general agreement with expectations from simple electron counting. The implications of these results for the unusual robustness of superconductivity and Kondo coherence with increasing x in this alloy system are discussed.

PACS numbers: 61.05.cj, 71.18.+y, 71.20.Dg, 71.27.+a, 75.20.Hr, 79.60.-i

I. INTRODUCTION

A. General Overview and Transport Properties

Heavy fermion (HF) systems are characterized by a delicate interplay of localized and itinerant electronic degrees of freedom that is responsible for a myriad of interesting strongly correlated electron phenomena¹. Here the localized f -electrons of Ce, Pr, Yb and various $5f$ elements embedded in an intermetallic compound hybridize with the conduction electrons².

The physics of the dilute limit of a single f -electron impurity in a metallic host is well-understood and described by the single-ion Kondo problem, where below the single ion Kondo temperature T_K the spins of the conduction electrons quench the local magnetic moment of the impurity via the Kondo interaction³. HF compounds represent the dense limit where the f -electron elements are arranged on a lattice, and in turn their local magnetic moments are mutually coupled through the conduction electrons by means of the Ruderman-Kittel-Kasay-Yosida (RKKY) interaction. The competition⁴ between RKKY and Kondo interactions is often summarized in a generic phase diagram for HF materials. On one end the RKKY interaction leads to the development of long-range antiferromagnetic (AFM) order. On the other end the Kondo interaction drives the demagnetization of the f -electron state, resulting in a paramagnetic HF state in which the entire lattice of f -electron moments collectively undergoes the Kondo effect and the f -electrons are delocalized into the conduction band⁵. The competing interactions can frequently be tuned by a non-thermal control parameter such as chemical composition

x , pressure P or magnetic fields H . A magnetic quantum critical point (QCP) is observed when the magnetic critical temperature is suppressed to zero.

Magnetic QCPs in HF compounds have continuously attracted scientific interest because in their vicinity the Fermi-liquid paradigm is observed to break down¹, frequently accompanied by the emergence of unconventional superconductivity (SC)⁶. Both phenomena originate from the abundance of soft magnetic quantum fluctuations at the QCP, which in the latter case are believed to provide the pairing “glue” for the SC⁷.

In particular, the family of tetragonal “115” systems has been investigated in great detail in order to disentangle the complex interplay between the heavy fermion state, unconventional SC and quantum criticality. The most prominent member of this class is CeCoIn_5 ⁸. CeCoIn_5 evinces superconductivity below a critical temperature $T_c = 2.3$ K, and is thought to be situated on the brink of an AFM QCP. This is reflected in the T -linear low-temperature electrical resistivity that indicates the presence of AFM quantum critical fluctuations⁹. Here magnetically mediated SC is supported by the observation of a strong spin-resonance in neutron scattering experiments¹⁰.

Apart from the SCing state, also the heavy normal state and non-Fermi liquid (NFL) properties of CeCoIn_5 have been studied extensively by tuning the system via rare earth substitution on the Ce site. Notably, an analysis of transport data for $\text{Ce}_{1-x}\text{La}_x\text{CoIn}_5$ introduced the notion of a coherence temperature $T^* \approx 45$ K below which f -electron delocalization is supposed to proceed¹¹. Further, for $\text{Ce}_{1-x}\text{R}_x\text{CoIn}_5$ it was found that both Cooper pair breaking and Kondo-lattice coherence are uniformly influenced by magnetic and nonmagnetic

rare earth (R) substituents. In contrast, the NFL behavior is strongly dependent on the f -electron configuration of the R ions¹². A more recent study suggests that the introduction of small amounts of non-magnetic impurities on the Ce (Y, La, Yb, Th) and In (Hg, Sn) site generates an inhomogeneous electronic state, in which the periodicity of the Kondo lattice is disrupted by the impurities¹³. This additionally results in a rapid local suppression of unconventional superconductivity.

These prior results can be contrasted with the properties of a new alloy series $\text{Ce}_{1-x}\text{Yb}_x\text{CoIn}_5$ for $0 \leq x \leq 1$ that may provide a fresh view on both the normal and the SCing state in HF compounds^{14,15}. Notably, it was found that the coherence temperature T^* , identified via the low-temperature electrical resistivity maximum, is essentially constant over the entire substitution range¹⁵. This is surprising by itself, but taking into account that the single ion Kondo temperatures T_K for CeCoIn_5 and YbCoIn_5 differ (see, e.g., Ref. 16), it also contradicts a recent study that suggests that T^* and T_K generally scale with each other¹⁷. The apparent stability of the electronic state is also reflected in the lattice parameters that remain nearly constant for $x \leq 0.775$, after which phase separation into Yb rich and deficient phases of $\text{Ce}_{1-x}\text{Yb}_x\text{CoIn}_5$ occurs. Also the magnetic susceptibility is almost unaffected by the substitution of Ce with Yb. The SCing critical temperature T_c decreases linearly with x towards 0 K as $x \rightarrow 1$, in contrast with other HF superconductors where T_c scales with T^* (see, e.g., Ref. 12). Only the low-temperature NFL behavior derived from the electrical resistivity, specific heat and magnetic susceptibility varies with x , even though there is no readily identifiable quantum critical point.

Two different hypotheses have been put forward to explain the remarkable behavior of $\text{Ce}_{1-x}\text{Yb}_x\text{CoIn}_5$. Based on the robustness of T_c and T^* , and most of all the agreement of the observed NFL behavior with the presence of critical valence fluctuations, Shu *et al.* have proposed a correlated electron state having cooperative valence fluctuations of Yb and Ce¹⁵. On the other hand, Booth *et al.*¹⁶ suggested from EXAFS measurements that below the Yb concentration where macroscopic phase separation takes place there is nonetheless a high degree of inhomogeneity in the form of large coexisting interlaced networks of CeCoIn_5 and YbCoIn_5 . It was argued that the YbCoIn_5 network would locally influence the physical properties of CeCoIn_5 , causing the slow suppression of T_c . But it seems that one could equally well imagine that the consequence of such large networks could be an unchanging value of T_c because the CeCoIn_5 and YbCoIn_5 networks would only influence each other at their respective surfaces. In that case, one would expect the T_c in the CeCoIn_5 network remains constant as function of Yb concentration, while the superconducting volume fraction for the entire sample would decrease. We also note that for the samples studied by Booth *et al.* a change in the distances of nearest neighbor ions has been observed for $x \sim 0.4$ using EXAFS. This may be interpreted as a

local precursor of the macroscopic phase separation that has been observed by Shu *et al.* at $x \sim 0.8$.

The implications of recent thin film studies are unclear for the issue of homogeneity. It was found for epitaxial superlattices of $\text{CeCoIn}_5/\text{YbCoIn}_5$ ¹⁸ that T_c is suppressed by $x \sim 0.2$, essentially like the behavior for other (R) substituents. For thin films of $\text{Ce}_{1-x}\text{Yb}_x\text{CoIn}_5$ ¹⁹ T_c is suppressed by $x \sim 0.4$, which is, on the one hand, smaller than for bulk crystals, but on the other hand, still larger than for other (R) substituents. One possible interpretation could be that the films are more homogeneous than the bulk crystals and thus show T_c suppression more quickly. But the more likely possibility is that the thin films constitute an essentially different materials system from the bulk crystals, e.g., owing to the effect of the interaction of the film with the substrate. For the thin films of $\text{Ce}_{1-x}\text{Yb}_x\text{CoIn}_5$ it was found¹⁹ that the in-plane lattice parameter is expanded slightly because it is in registry with the substrate and does not change with x , whereas the out-of-plane lattice parameter varies linearly with x between the values for CeCoIn_5 and YbCoIn_5 , quite different from the behavior of the bulk crystals.

Both hypotheses, the cooperative valence fluctuations as well as the coexisting interlaced networks, have interesting implications and justify a more detailed microscopic investigation of the electronic structure, and in particular the Ce and Yb valences. The possibility of critical valence fluctuations within an extended SCing phase is remarkable in the context of recent studies in which CeRhIn_5 ²⁰ and CeCu_2Si_2 ²¹ were suggested as candidates for valence-fluctuation mediated SC. Further a recent study of the transport properties of CeRhIn_5 under hydrostatic pressure found that scattering of the charge carriers near the AFM QCP is isotropic, in contrast to expectations for a classical AFM QCP. This finding was interpreted as a signature of coexisting critical degrees of freedom in both spin and charge channels²² that could be a source of SC pairing. On the other hand SC in interlaced networks of CeCoIn_5 and YbCoIn_5 is of interest in view of a current proposal that unconventional SCs in the vicinity of AFM may be generally electronically textured²³. Finally, the x -dependence of T^* has been addressed in a recent theoretical work which demonstrates that the onset of coherence is strongly affected by the degree of correlations between impurity sites²⁴.

B. Issues of valence and electron counting

With the proposal of cooperative valence fluctuations, the x -dependencies of the Ce and Yb valences are of immediate interest. From spectroscopic information and analysis of bulk properties the $x = 0$ compound is known to have essentially trivalent Ce ($4f^1$) and the uncorrelated behavior of the $x = 1$ compound might suggest divalent Yb ($4f^{14}$). But the picture of cooperative valence fluctuations in the alloy would require intermediate

valence Yb. This picture has been supported by a report from Booth *et al.*¹⁶ from X-ray absorption spectroscopy (XAS) at the Yb and Ce L_{III} edges that the Yb and Ce valences are $\tilde{2}.3$ and $\tilde{3}.1$, respectively. Ref. 16 also finds these valences to be essentially independent of x . The $x = 1$ compound can then be interpreted¹⁶ as intermediate valence with the $4f^{13}$ magnetic moment quenched on such a high energy scale T_K that Curie Weiss behavior cannot be seen. T_K was estimated in Ref. 16 to be larger than 6000 K.

There are also important questions of electron counting and the implications for the volume contained by the Fermi surface (FS). It must be kept in mind that if a local moment is quenched, e.g., by the Kondo effect, then the electrons producing the moment must be included in the Fermi surface (FS). Thus for Ce^{3+} with its magnetic moment Kondo quenched, the FS volume is based on an atomic configuration $[Xe]4f^{15}d^{16}s^2$ having 4 delocalized electrons/Ce, the same as if Ce were formally Ce^{4+} $[Xe]4f^05d^26s^2$. For $CeCoIn_5$ de Haas van Alphen (dHvA) measurements^{25–27} at low temperatures have found that the $4f$ electron is included in the Fermi surface although angle resolved PES (ARPES) performed at $\tilde{2}0K$ has found the FS expected in LDA band calculations with the Ce $4f$ electron confined to the core, i.e. $[Xe][4f^1]5d^{16}s^2$ with 3 electrons/Ce going into the FS.^{28,29} Analogously for Yb^{3+} with $4f^{13}$, if the magnetic moment of the $4f$ hole is quenched, the Fermi surface must contain the $4f$ hole and so its volume will be the same as though Yb were formally divalent $[Xe][4f^{14}]6s^2$, i.e., the FS volume would contain 2 electrons/Yb. Because of its large T_K this situation is expected up to very high temperatures for $YbCoIn_5$. Thus, no matter whether or not the $4f$ electron in $CeCoIn_5$ is localized at the measurement temperature, one expects that in comparing the $x = 1$ and the $x = 0$ compounds, characteristic hole FS features will tend to expand and characteristic electron FS features will tend to shrink with increasing x .

Recent dHvA experiments³⁰ found that the FS of $YbCoIn_5$ is indeed much different from that of $CeCoIn_5$. The measured frequencies are in reasonable agreement with an LDA calculation for $YbCoIn_5$, which gives an Yb valence of 2.3, the same as found in XAS¹⁶, and shows reduced volume relative to that of $x = 0$. For example the frequencies assigned to two prominent electron FS features centered on the M-A line in k -space and known as α and β from LDA^{25,31} and dHvA^{25–27} studies for $x = 0$, decrease markedly from $x = 0$ to $x = 1$. It is also of note that the dHvA effective masses for $YbCoIn_5$ are relatively small, in the range $1.0 m_e$ to $1.5 m_e$. These small masses are consistent with the very large value of T_K implied¹⁶ by the Yb valence of 2.3. For $x = 0.1$, the dHvA frequencies and masses are unchanged from those of $x = 0$ and for $x = 0.2$ there appear frequencies characteristic of both $x = 0$ and $x = 1$. For $x = 0.55$, the next highest value for which dHvA data were obtained, and for higher values $x = 0.85$ and 0.95 , the frequencies and

masses that could be observed are generally like those that are found for $x = 1$, with the α frequencies essentially unchanged and the β frequencies changing slightly. Thus dHvA shows a rather abrupt change of electronic structure around $x = 0.2$. In contrast, Ref. 16 reported from ARPES that the electronic structure along the Γ -M line is essentially invariant with x , including $x = 1$.

C. Present work and Organization of the Paper

In the present work we determine the Ce valence from XAS at the Ce $M_{4,5}$ edges and the Yb valence from $4f$ electron x-ray photoemission spectroscopy (XPS). In agreement with Ref. 16, we find that the Ce valence is near 3+ and essentially independent of x . The Yb valence for $x = 1$ and decreasing to $\tilde{0}.3$ is $\tilde{2}.3$, also in agreement with the finding of Ref. 16. But as x decreases further and approaches 0 the valence increases to nearly 3+. We also report and analyze the x -dependence of the alloy magnetic susceptibility for temperatures where it exhibits Curie-Weiss behavior, and we introduce a simple model to inter-relate the effective moment and the Ce and Yb valences. Under the assumptions that Kondo effects can be ignored and that the Ce valence is essentially 3+, we infer Yb valences in very good agreement with the values found from XPS, including their tendency to increase toward 3+ for small x . The x -dependencies of the valences can also be combined with atomic radii information to predict x -dependent unit cell volumes that are in fair agreement with the measured values. Thus the rather abrupt change of electronic structure found in dHvA can now be seen as resulting from a change of Yb valence.

We present the k -dependent electronic structure and FS of $CeCoIn_5$ and $YbCoIn_5$ throughout the Brillouin zone as measured using variable photon energy ARPES. In contrast to the results of Ref. 16 we find along the Γ -M line a large difference of electronic structure for $x = 0$ and $x = 1$. In particular the sizes of the α and β sheets decrease markedly from $x = 0$ to $x = 1$, in good qualitative agreement with the general expectations from electron counting set forth above and with the dHvA results³⁰. But in disagreement with dHvA is the observation of a smaller, essentially proportionate, size change of the α sheet for $x = 0.2$. The somewhat columnar shapes of these FS features have drawn attention in connection with the idea that the layered crystal structure may be important for the SC of the $x = 0$ compound.

The remainder of the paper is organized as follows. The experimental details on the sample preparation, bulk property measurements and spectroscopic measurements are summarized in section II. Section III presents the various spectroscopic studies and the data analysis used to determine the Yb and Ce valences. In section IV we relate the Ce and Yb valences to the dependence of the magnetic susceptibility and the unit cell volume on the Yb concentration x . Our ARPES results for $x = 0$,

0.2 and 1 are presented in section V. We end with a summary and our conclusions in section VI.

II. EXPERIMENTAL DETAILS

Single crystals of $\text{Ce}_{1-x}\text{Yb}_x\text{CoIn}_5$ were grown using an indium self flux method^{32,33}. High purity elements (Ce, 3N; Yb, 3N; Co, 3N; In, 4N) were placed in alumina crucibles and heated in quartz tubes with 150 psi argon gas. The heating schedule consisted of an initial ramp at 50 °C/hr to 1050 °C, a dwell at 1050 °C for 72 hours, and a two-stage cooling process to avoid forming crystals of CeIn_3 – first a rapid cooling from 1050 °C to 800 °C followed by a slow cool to 450 °C, where the excess flux was spun off in a centrifuge.³³ The resulting crystals were characterized with x-ray powder diffraction (XRD) and energy dispersive x-ray (EDX) analysis in order to verify both the correct structure and composition. The magnetization M_{ab} of the crystals was measured as a function of temperature for $2 \text{ K} \leq T \leq 300 \text{ K}$ using a Quantum Design superconducting quantum interference device (SQUID) magnetometer in a magnetic field $H = 5000 \text{ Oe}$ applied parallel and perpendicular to the basal tetragonal plane.

The spectroscopic measurements XAS, XPS and ARPES were performed at undulator beamline 7.0.1 of the Advanced Light Source (ALS) synchrotron. XAS was measured using total electron yield (TEY), by simultaneously measuring the sample current and the reference of a Ni mesh located before the sample in the monochromator. A Scienta R4000 electron spectrometer with 2D parallel detection of electron kinetic energy and angle in combination with a highly-automated six-axis helium cryostat goniometer was used to acquire Fermi surface (FS) and electronic structure maps with a wide $>30^\circ$ angular window covering multiple Brillouin zones (BZs). The measurements were performed with pressure between $8 \times 10^{-11} \text{ mbar}$ and $1 \times 10^{-10} \text{ mbar}$. The samples were cleaved *in situ* by pushing against a post which was glued on the sample surface by epoxy adhesive. The cleavage temperature was between 20 K and 25 K, essentially equal to the measurement temperature, which was 25 K for CeCoIn_5 and 20 K for YbCoIn_5 . The position of the Fermi energy and the energy resolution were determined by measuring a gold foil adjacent to and in good thermoelectrical contact with the sample. Before measuring, the gold foil was scraped *in situ* to obtain a clean surface. Within about 100 μm all spectroscopic data were collected on the same spot of the cleavage plane, which showed no visible inhomogeneities either *in situ* or afterwards in images in both an optical microscope and an electron microscope.

XAS measurements had a resolution of 250 meV. For XPS, the overall energy resolution was set to 140 meV FWHM for photon energies of $h\nu = 550 \text{ eV}$ and 250 meV for photon energies of $h\nu = 865 \text{ eV}$. For ARPES the total energy resolution of the analyzer and exciting pho-

tons varied from 30 meV at $h\nu = 80 \text{ eV}$ to 45 meV at $h\nu = 200 \text{ eV}$, and the angular resolution of 0.3° corresponds to a parallel angular momentum resolution range of 0.024 \AA^{-1} to 0.037 \AA^{-1} . Detector angular distortions are corrected using calibration data acquired with a slit array placed between the sample and analyzer lens. Angular and photon-dependent Fermi-energy maps were extracted with an energy width of 50 meV. The value of k perpendicular to the sample surface (k_z) could be selected by varying the photon energy, as verified and calibrated from repeating features in k_z - k_x maps using a standard method³⁴ that approximates the photoelectron dispersion by a free electron parabola and an "inner potential" V_0 to characterize the surface potential discontinuity. A V_0 value of $11.9 \pm 0.6 \text{ eV}$ best describes the repeating features in the data.

After performing the electron spectroscopy, we obtained the actual composition of the $\text{Ce}_{1-x}\text{Yb}_x\text{CoIn}_5$ crystals by X-ray energy dispersive spectrometry analysis (XEDS). The analysis was performed at the Electron Microbeam Analysis Laboratory at the University of Michigan. In the scanning electron microscope, it is possible to use a focused probe to determine the composition of the sample at a resolution of a few μm (the actual value depends on the average atomic number of the sample and the accelerating voltage of the microscope). In this experiment the accelerating voltage was 30 kV. The area analyzed by electron spectroscopy was analyzed by XEDS with the probe scanning the same area analyzed by the synchrotrons beam spot, roughly 50-100 μm . No Yb inhomogeneities were detected within the measured area. The composition analysis was performed by measurement of the In L-lines, the Ce L-lines, the Co K-lines and the Yb-L lines. Atomic number, absorption and fluorescence (ZAF) correction was applied. The end-members CeCoIn_5 and YbCoIn_5 were used as standards in order to produce correction factors for composition determination.

III. CE AND YB VALENCES FROM SPECTROSCOPY

A. XAS for Ce valence

In order to determine the change of the Ce valence upon doping, we performed TEY XAS near the Ce M_4 and M_5 edges. In this experiment we look at the $3d^{10}4f^0 \rightarrow 3d^9 4f^1$ and $3d^{10}4f^1 \rightarrow 3d^9 4f^2$ absorption lines, which are further separated accordingly to the core hole being $3d_{5/2}$ (M_5) or $3d_{3/2}$ (M_4). Because the d core-hole interacts strongly with the promoted f-electron, this absorption results in strong excitonic lines at energies below the true $3d \rightarrow 6p$ absorption edges, with characteristic structure due to multiplet splittings of the final states. In the two topmost curves of Fig. 1 (a), we show an atomic multiplet calculation³⁵ for the initial state (final state) being f^0 (f^1) or f^1 (f^2).

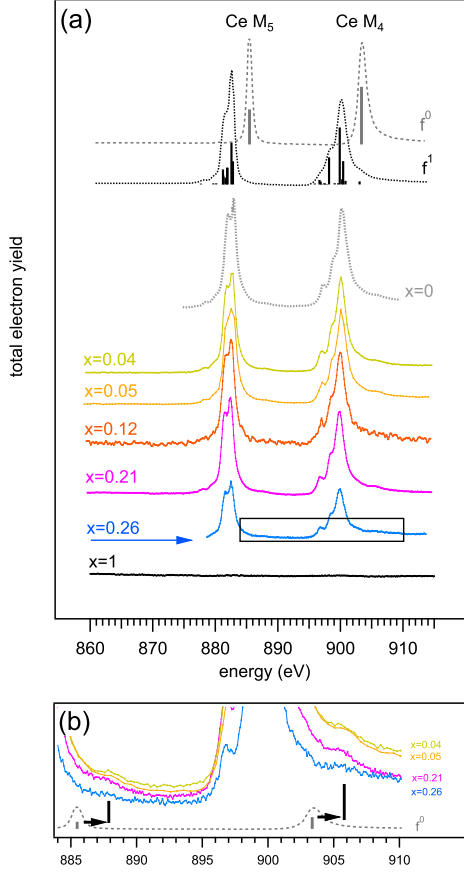


FIG. 1: (a) X-ray absorption measurements at $T = 20$ K near the Ce M_4 and M_5 edges show that Ce is essentially trivalent. The topmost curves, labeled on the right side with f^0 or f^1 are multiplet calculation³⁵. Below are measured spectra for the series $Ce_{1-x}Yb_xCoIn_5$. The curve for $x = 0$ is from Ref. 39. The box in (a) indicates the region displayed in (b) which is the magnification of the low intensity region where the f^0 -component shows up.

A mixed valence system shows absorption lines of both valences. The intensity ratio $R = I(f^0)/[I(f^0) + I(f^1)]$, where $I(f^0)$ and $I(f^1)$ are the integrated intensities for lines with initial states f^0 and f^1 , respectively, is a measure of the initial state f^0 component ($1-n_f^{Ce}$), where n_f^{Ce} is the Ce $4f$ occupancy. There are, however, the following caveats. First, within the framework of the Anderson impurity model, R underestimates ($1-n_f^{Ce}$) due to the mixing of the f^1 and f^2 final states through the hybridization of the f -states with the conduction electrons^{36,37}. Second, TEY detection has a contribution from the surface, which can have smaller ($1-n_f^{Ce}$) than the bulk because the hybridization can be reduced and the $4f$ binding energy increased relative to the bulk. Generally, the total fluorescence yield is more bulk sensitive than TEY and also tends to enhance the f^0 peak due to the bulk self-absorption of the much stronger Ce

f^1 -component. The greatest sensitivity to the f^0 component is achieved through XAS on L_{III} edges and resonant x-ray emission³⁸. Thus really precise absolute values for the Ce valence are not accessible here. Nonetheless the $M_{4,5}$ spectra are known to be a very reliable qualitative guide to $(1-n_f^{Ce})$ and are very accurate for the main purpose here of detecting a relative change with x if it exists.

The lower curves in Fig. 1 (a) show experimental XAS results, all at $T = 20$ K, for the series $Ce_{1-x}Yb_xCoIn_5$. The curve for $x = 0$ is from Ref. 39 and indicates therefore reproducibility of the results. Our spectra were normalized at the background from $h\nu = 910$ eV to $h\nu = 915$ eV. The spectrum for $x = 1$ shows expectedly no Ce signal. For $x < 1$, the spectra are dominated by the f^1 -component with only a small f^0 -satellite. In Fig. 1 (b), we show a magnification of the low intensity region. At about $h\nu = 888$ eV and $h\nu = 906$ eV, there are little humps due to the f^0 -component. Also one can see in that magnification that the (dotted) curve from the atomic multiplet calculation for f^0 has to be shifted by about +2.5 eV to account for increased screening in the solid state. Overall, the measured curves do not strongly change with x . We can safely conclude, in agreement with Ref. 16, that Ce is essentially trivalent and unchanging for the whole measured series. As a quantitative measure of a possible valence change of the Ce, we determined the intensity of the f^1 -component by a fit with five Gaussians for M_5 and four Gaussians for M_4 . Similarly, we determined the f^0 -component by one Gaussian each for M_5 and M_4 . Thereby we find at $T = 20$ K that the value of R is essentially constant at 0.04 ± 0.04 and 0.1 ± 0.12 for M_5 and M_4 , respectively.

B. 4f PES for Yb valence

In order to elucidate the valence of the Yb, we analyze $4f$ XPS spectra. At the beginning of our measurements, we routinely confirm the absence of oxygenated surfaces by taking scans over a large binding energy region that includes the core-states as shown in the inset of Fig. 2 (a). These wide scans also offer the opportunity to normalize our valence-band spectra by assuming that each photon energy the area of the In- $3d$ peaks is constant for the whole series of $Ce_{1-x}Yb_xCoIn_5$. We show such normalized valence band spectra for the photon energy of $h\nu = 865$ eV in Fig. 2 (a). The data are stacked with a constant shift in intensity and are ordered with increasing Yb concentration from bottom to top, i.e. the lowest is $x=0.04$ followed by $x=0.05, 0.12, 0.21, 0.26, 1$. The first notable feature, which we label in the spectra, is the final state $^2F_{5/2} - ^2F_{7/2}$ doublet of the Yb^{2+} photoemission process $4f^{14} \rightarrow 4f^{13}$. This feature is quite intense because the large number of fourteen Yb f -electrons causes a much stronger photoemission signal compared to those of Ce, In, or Co. Tuning the photon energy to the M_5 resonance at $h\nu = 883$ eV (compare also with Fig. 1) allows us to see the Ce-weight as shown in

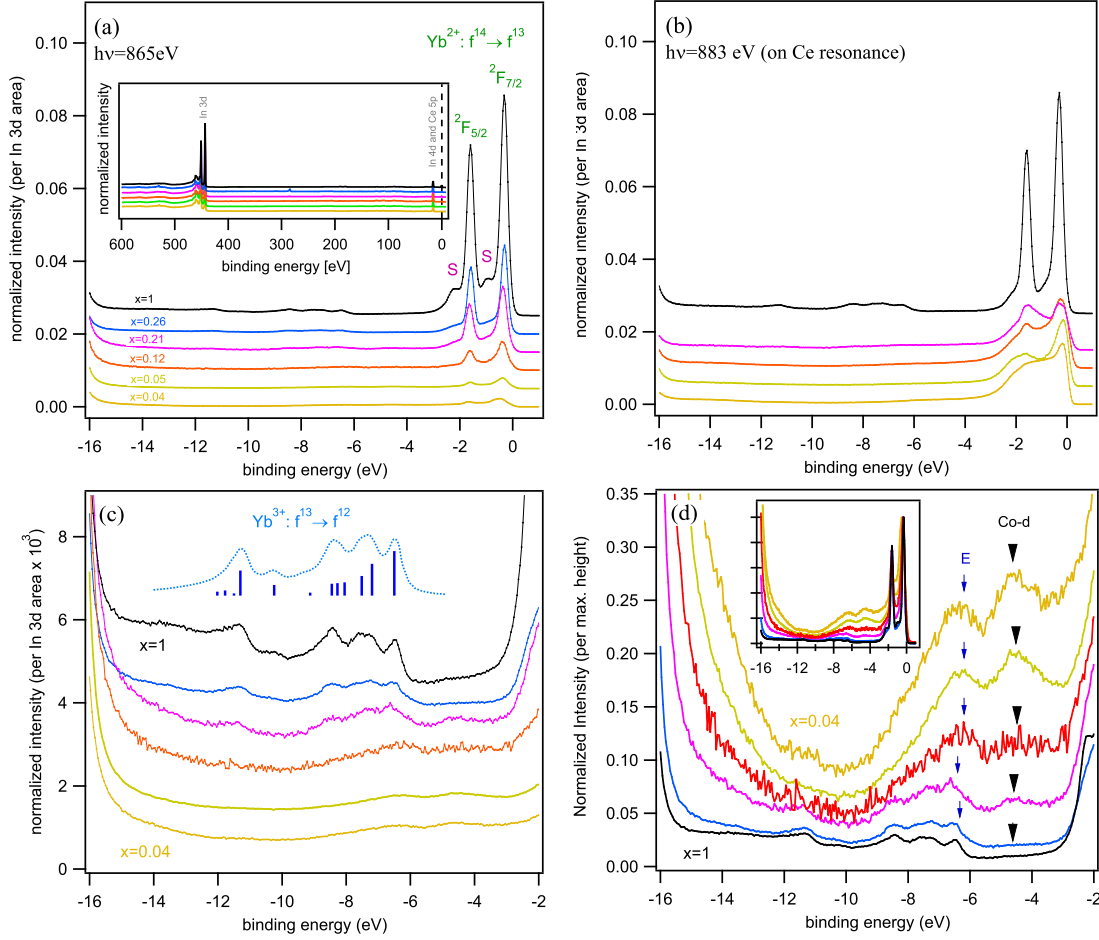


FIG. 2: XPS spectra of the $\text{Ce}_{1-x}\text{Yb}_x\text{CoIn}_5$ samples at $T=20$ K. The spectra are sorted by their nominal Yb content. Except for the reversed order in (d), the topmost spectrum is for $x=1$ and the bottom one is for $x=0.1$. (a) Spectra of the valence band region near the Fermi energy taken at $h\nu=865$ eV. The doublet labeled $2F_{5/2} - 2F_{7/2}$ is due to bulk Yb^{2+} . The two peaks due to surface Yb^{2+} are labeled 'S'. The inset of (a) shows a wide scan over a large binding energy region. This spectrum is dominated by the In 3d doublet which was used to normalize the spectra. Near the Fermi-energy, a peak originating from In 4d and Ce 5p is visible. (b) Spectra of the same valence band region as in (a) but on the Ce resonance at photon energies of $h\nu=883$ eV. This increases the visibility of the Ce component in the spectra. Panel (c) shows a magnification of the region in the spectra of (a) where the Yb^{3+} component can be detected. The topmost curve is a theoretical calculation for the $\text{Yb}^{3+} 5f^{13} \rightarrow 5f^{12}$ spectrum from Ref. 40. (d) is the same spectrum as (c) but normalized to the maximum of the $2F_{7/2}$ -peak as shown in the inset. The peak maximum originating from Co-d weight and the low energy edge "E" of the $\text{Yb}^{3+} 5f^{13} \rightarrow 5f^{12}$ multiplet are marked.

Fig. 2 (b). As expected we see that this Ce weight decreases upon adding more Yb although the Yb^{2+} doublet is still very strong as seen by comparing the intensity for the $x=1$ sample, which certainly has no Ce weight, with the Ce-signal enhanced intensity for all spectra for $x < 1$. Going back to Fig. 2(a), the second notable feature is two lower intensity peaks which are marked by 'S' above them. These two peaks show the same energy separation between each other as the separation of the $2F_{5/2} - 2F_{7/2}$ doublet described above. Thus they are also due to Yb^{2+} but instead of coming from the bulk this signal comes from the surface. The absence of ligand-atoms

causes a stronger screening of the f -levels and therefore the spectrum shifts down in energy. Such surface shifted Yb^{2+} peaks are well known.

The third feature in the spectrum, finally, is of lower intensity and can be better seen in Fig. 2 (c), which shows a magnification of the interesting region. Although the structure consists of many peaks their mutual origin is from Yb^{3+} for which the photoemission process $5f^{13} \rightarrow 5f^{12}$ gives a final state multiplet of thirteen lines. The topmost curve serves as a fingerprint for Yb^{3+} as it represents a calculation of this multiplet structure using intermediate coupling⁴⁰. Counting the lines of this multiplet, one finds only twelve. The missing line is from a

1S state at $\tilde{16.3}$ eV binding energy, which causes it to be merged with the strong signal of the In 4d and Ce 5p doublets. For our later quantitative discussion, it is good to note that, according to the calculation, this line has only about 0.09/13 $\tilde{0.7}$ % of the total intensity of the multiplet and is therefore quite negligible. We notice in Fig. 2 (c) that, as we would expect, the intensity of the Yb^{3+} -signal decreases as the concentration of Yb decreases. This however does not necessarily mean that the Yb valence has to change.

Before we start to evaluate the Yb valence qualitatively, we note that there is a relatively easy method to graphically visualize the Yb valence by normalizing the data in a different way. In Fig. 2 (d) we show the same spectra as in (c) and (a), at $h\nu=865$ eV, but with another normalization. This normalization just divides the spectrum by the maximum intensity of the $^2F_{7/2}$ peak. For $x < 1$ there is Ce-weight buried under these peaks. Thus we are overestimating the Yb^{2+} component for smaller x . There is one feature which is more revealed as the absolute intensity of the Yb-related features is more and more decreased. It is marked with an arrow and it stems from the Co d-states. This growing of the Co-d related weight shifts the edge "E" of the foremost part of the Yb^{3+} multiplet up. Taking the height between the edge "E" and the dip located between E and the Co-d peak, we can qualitatively state that for $x=1$ the Yb^{2+} component is strong. We can also clearly see that the Yb^{3+} component has a lower intensity for $x=1$ and $x=0.26$ than it has for $x < 0.26$. This is even true without taking account of the fact that the normalization overestimates the Yb^{2+} component for low x .

In order to quantitatively extract the Yb valence, we applied a fitting procedure presented in Fig. 3. The background used was a Shirley-like background and, additionally, a linear background which simulates the contribution coming from the In 4d and Ce 5p doublets at higher binding energies. We modeled the $F_{5/2} - F_{7/2}$ doublet of the bulk Yb^{2+} as two Lorentzians with the fixed intensity ratio 6:8. The Yb^{2+} surface component was modeled similarly. We reduced the twelve $\text{Yb}^{3+} 5f^{13} \rightarrow 5f^{12}$ lines to 7 Lorentzians. The weights and positions of these Lorentzians relative to each other were determined at $x = 1$ (see inset of $x = 1$ in Fig. 3). For fitting the other Yb concentrations, we allow only the relative intensities of the two valence components to change. The fitting routine first finds the bulk Yb^{2+} -component and the Yb^{3+} component together with the background, adds then the surface Yb^{2+} , and after that subsequently adds just enough extra peaks to optimally fit the spectrum. These extra peaks are mainly to simulate the contributions of Co-d and Ce-f. For these extra peaks, we took two or three Lorentzians. All spectral features were convolved with a Gaussian having the FWHM of the resolution. Having so many components for a line-fit, we may not always correctly distinguish between the surface Yb^{2+} -component and these extra peaks. However, as can be seen in Fig. 3, the peaks labeled as 'rest' represent

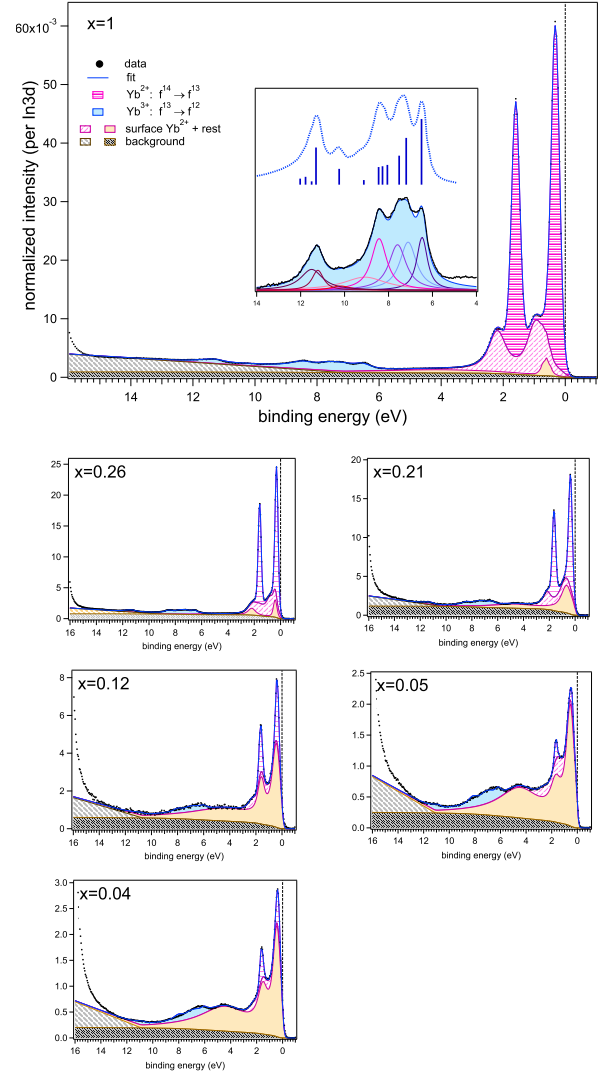


FIG. 3: Example of the line-fits performed in order to determine the Yb-valence. The spectra shown are the same as in Fig. 2 (a), at $h\nu = 865$ eV. For the fit, we divided the spectrum into components from Yb^{2+} , surface Yb^{2+} and Yb^{3+} . Furthermore, we use a Shirley background and a linear background and some subsequently added Lorentzians, just enough to optimally fit the spectrum (denoted as 'rest'). The inset of $x = 1$ shows the 7 Lorentzians we used to model the the twelve $\text{Yb}^{3+} 5f^{13} \rightarrow 5f^{12}$ lines.

very much what would be expected from the Co and Ce weights. For these Ce weights, the reader can compare with Fig. 2 (c).

The result of the fitting procedure is summarized in Fig. 4. There, we plot the fitting result for both photon energies. The fact that the results are essentially the same for both photon energies assures us that the fit is finding the amount of the surface Yb^{2+} -component correctly and that the valence obtained here reflects that of the bulk. For the general trend of the valence vs. Yb concentration we see that the Yb valence is near $3+$ at very

low x and goes down to about +2.3, as already concluded qualitatively from Fig. 2. Compared to the results of Ref. 16, we obtain the same valence of about +2.3 for the end-member $x = 1$. As discussed in Ref. 16 the intermediate valence of the end-member together with the nonmagnetic behavior seen in its magnetic susceptibility¹⁵ indicates that YbCoIn₅ has a very high single ion Kondo temperature T_K . However, by measuring for lower x -values than in Ref. 16, we obtain the new result that the Yb valence is strongly increasing to trivalent for small values of x going to zero. We will see in the next section that an analysis of the valence from bulk properties is consistent with the rather abrupt increase of valence at low x observed spectroscopically. As noted already in Section IB this change of Yb valence is also in good agreement with the change of electronic structure observed in dHvA experiments³⁰.

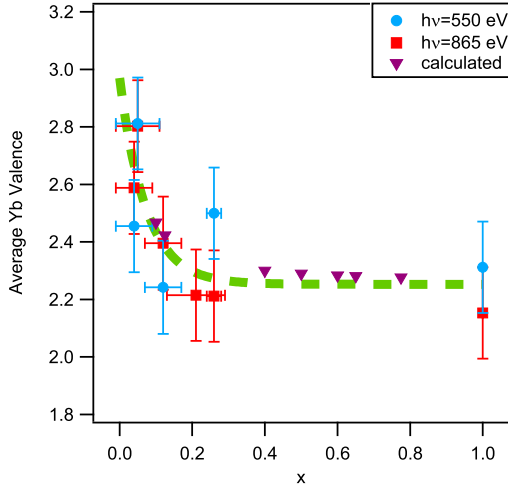


FIG. 4: x -dependence of Yb valence from the XPS spectra at photon energies of $h\nu = 550$ eV and $h\nu = 865$ eV. The line is a guide to the eye. Open circles are the calculated Yb valences from the susceptibility analysis of the next section using Eq. 4.

IV. RELATION OF CE AND YB VALENCES TO BULK PROPERTIES

Figure 5(a) shows the inverse magnetic susceptibility $\chi_{ab}^{-1}(T) = H/M_{ab}(T)$ of $\text{Ce}_{1-x}\text{Yb}_x\text{CoIn}_5$ in the normal state vs. Yb concentration x . The data were collected by warming the sample gradually after zero-field cooling (ZFC), and subsequently field cooling (FC). The difference between the ZFC and FC data is negligible. Above $T \approx 30$ K and for all x the magnetic susceptibility of χ_{ab} of $\text{Ce}_{1-x}\text{Yb}_x\text{CoIn}_5$ follows a Curie-Weiss law

$$\chi_{ab} = N_A \mu_{\text{eff}}^2 / 3k_B (T - \theta_{\text{CW}}), \quad (1)$$

where N_A is Avogadro's number and k_B is Boltzmann's constant. The effective magnetic moment μ_{eff} and the

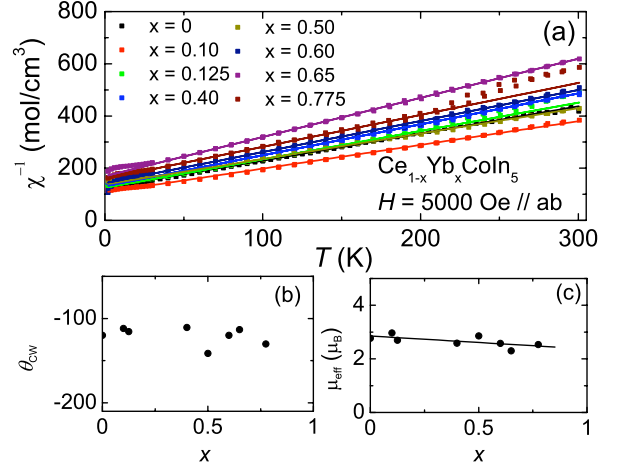


FIG. 5: (a) Inverse magnetic susceptibility $\chi_{ab}^{-1}(T) = H/M_{ab}(T)$ vs. temperature T along the crystallographic ab plane for $\text{Ce}_{1-x}\text{Yb}_x\text{CoIn}_5$ with Yb concentrations $0.0 \leq x \leq 0.775$. Curie-Weiss temperature θ_{CW} and effective magnetic moment μ_{eff} as determined from fits to a Curie-Weiss law $\chi_{ab} = N_A \mu_{\text{eff}}^2 / 3k_B (T - \theta_{\text{CW}})$ (please see text) as function of Yb concentration x are shown in (b) and (c), respectively. Solid line in (c): linear fit of $\mu_{\text{eff}}(x)$.

Curie-Weiss temperature θ_{CW} as determined from fits of the data (solid lines in Fig. 5(a)) to Eq. 1 are shown in Fig. 5(b) and (c). Without taking into account modifications of the susceptibility due to crystal-electrical-field (CEF) effects, Kondo effect, valence fluctuations, etc., the fits yield $\theta_{\text{CW}} \approx -120$ K independent of Yb concentration to first approximation (Fig. 5(b)). Curie-Weiss behavior is also observed in temperature dependence of magnetic susceptibility χ_c at high temperatures ($T \geq 50$ K), and the fits give similar values of μ_{eff} and θ_{CW} .

The magnetic susceptibility $\chi(x)_{ab}$ of $\text{Ce}_{1-x}\text{Yb}_x\text{CoIn}_5$ is composed of two contributions arising from Ce and Yb ions, respectively,

$$\chi(x)_{ab} = \chi_{\text{Ce}}(1-x) + \chi_{\text{Yb}}x. \quad (2)$$

Using that θ_{CW} is independent of x (cf. Fig. 5(b)), we can write

$$\mu_{\text{eff}}^2(x) = \mu_{\text{Ce}}^2(x)(1-x) + \mu_{\text{Yb}}^2(x)x. \quad (3)$$

Following the conclusion of the previous section and of Ref. 16 we take the f -electron orbital occupancy for Ce to remain close to 1 ($n_f^{\text{Ce}} \approx 1$), i.e., the Ce ions remain 3+ for all x . Thus, by assuming that $\mu_{\text{Ce}}(x) = \mu_{\text{Ce}3+} = 2.54 \mu_B$ for all x and approximating $\mu_{\text{eff}}(x)$ by the linear fit illustrated in Fig. 5(c), we can estimate $\mu_{\text{Yb}}(x)$ by using Eq. (3). The f -hole occupancy for Yb is given by $n_f^{\text{Yb}}(x) = \frac{\mu_{\text{Yb}}^2(x)}{\mu_{\text{Yb}3+}^2}$, where $\mu_{\text{Yb}3+} = 4.54 \mu_B$. Accordingly, the effective valence is then obtained as

$$v_{\text{Yb}}(x) = 2 + n_f^{\text{Yb}}(x). \quad (4)$$

As shown by the open circles in Fig. 4, the result is in surprisingly good agreement with the results of the XPS measurements, considering the simplicity of analysis of the magnetic susceptibility.

There is a well-known correlation between lattice parameters and valence in f-electron materials⁴¹. For the system $\text{Ce}_{1-x}\text{Yb}_x\text{CoIn}_5$, which has a tetragonal crystal structure with basal plane and interplane lattice parameters a and c , respectively, we consider the relationship between the unit cell volume $V = a^2c$ and the valences

$$\begin{aligned} V(x) &= V_{\text{Ce}^{3+}}(1-x) + V_{\text{Yb}}x \\ &= V_{\text{Ce}^{3+}}(1-x) + [V_{\text{Yb}^{3+}} + [V_{\text{Yb}^{2+}} - V_{\text{Yb}^{3+}}](1 - n_f^{\text{Yb}}(x))]x \\ &= 159.9 \text{ \AA}^3(1-x) + [155.6 \text{ \AA}^3 - 3.6 \text{ \AA}^3 n_f^{\text{Yb}}(x)]x. \end{aligned} \quad (5)$$

The values of the unit cell volumes used in this expression are $V_{\text{Ce}^{3+}} = 159.9 \text{ \AA}^3$, $V_{\text{Yb}^{2+}} = 155.6 \text{ \AA}^3$, and $V_{\text{Yb}^{3+}} = 152.0 \text{ \AA}^3$, while $n_f^{\text{Yb}}(x)$ is the number of holes in the Yb 4f-electron shell ($n_f^{\text{Yb}}(x) = 1$ for Yb^{3+} and 0 for Yb^{2+}). The value of $V_{\text{Yb}^{3+}}$ was estimated by interpolating the values of $V_{\text{Ln}^{3+}}$ from the neighboring LnCoIn_5 compounds with trivalent Ln ions⁴² to YbCoIn_5 . The value of $V_{\text{Yb}^{2+}}$ was estimated using the value of $V_{\text{Yb}^{3+}}$ and $V_{\text{Yb}^{2.3+}}$, inferred from the XAS data reported herein for the compound YbCoIn_5 , using the term for V_{Yb} in brackets in Eq. 5, which yields

$$V_{\text{Yb}^{2+}} = [V_{\text{Yb}}(x) - V_{\text{Yb}^{3+}} n_f^{\text{Yb}}(x)] / [1 - n_f^{\text{Yb}}(x)]. \quad (6)$$

Using $n_f^{\text{Yb}}(1) = 0.3$ for $x = 1$, we obtain $V_{\text{Yb}^{2+}} = 155.6 \text{ \AA}^3$ from Eq. 6.

In Fig. 6, we compare $V(x)$ determined from Eq. 5 with the values obtained from the XRD measurements on $\text{Ce}_{1-x}\text{Yb}_x\text{CoIn}_5$. It can be seen that the calculated values of $V(x)$ are nearly linear and generally conform to the behavior expected from Vegard's law for Ce^{3+} and $\text{Yb}^{2.3+}$. The calculated values of $V(x)$ are smaller than the measured values, and the discrepancy is larger for larger values of x . A number of factors could contribute to this discrepancy; e.g., (1) Weakening of the metallic bond due to the decrease in the conduction electron density with Yb concentration that accompanies the substitution of Yb ions (valence $2.3+$) for Ce ions (valence $3+$), resulting in an increase of the unit cell volume, (2) a non-linear contribution considered by Varma and Heine⁴³ in calculating the unit cell volume for Ln compounds with intermediate valence, and (3) a reduction of the actual Yb concentration compared to the nominal concentration.

of the Ce and Yb ions. The lattice parameters a (c) for CeCoIn_5 and YbCoIn_5 determined from XRD measurements are 4.6012 \AA (7.5537 \AA) and 4.5590 \AA (7.433 \AA),¹⁵, respectively, and the valence of Ce and Yb as obtained by our photoemission measurements and calculations are $\tilde{3}+$ and $\tilde{2.3}+$, respectively. This yields unit cell volumes of $V = 159.9 \text{ \AA}^3$ for CeCoIn_5 and 154.5 \AA^3 for YbCoIn_5 . Assuming that Vegard's law applies to the unit cell volume V as a function of x and that the valence of Ce remains near $3+$ for all values of x , $V(x)$ can be expressed as

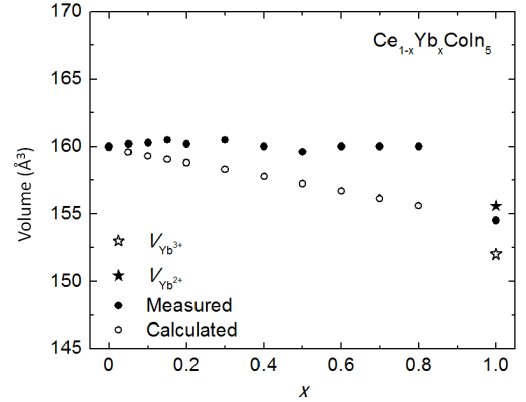


FIG. 6: Unit cell volume V as a function of Yb concentration x in $\text{Ce}_{1-x}\text{Yb}_x\text{CoIn}_5$. Filled circles: measured values of V . Open circles: calculated V using Eq. 5. Open circles: calculated V using Eq. 5.

V. ELECTRONIC STRUCTURE FROM ARPES

In this section we present and discuss the rather columnar α and β FS sheets for $x = 0, 0.2$ and 1 as inferred from variable photon energy ARPES FS maps. Thus far ARPES data of sufficiently high quality have not been obtained for other values of x . In that connection we note that it was also challenging to obtain dHvA spectra for intermediate values of x , attributed in Ref. 30 to increased scattering rates in the alloys as inferred from Dingle temperatures that increased considerably from $x = 0$ to $x = 0.55$. Such disorder would also degrade the sharpness of ARPES FS maps.

The three lowest rows of Fig. 7 show maps for $x = 0$,

0.2 and 1 measured at 26 K, 26 K and 20 K, respectively. Higher intensity correlates with darker color in these maps. We show two interesting cuts through the high symmetry points of the three dimensional Brillouin-zone (BZ). One cut contains the Γ -point (left) and the other the Z-point (right). The orientation of these two planes within the BZ is sketched in the center of the upper panel of the figure.

There are many details visible in these six FS maps and furthermore they represent only a small fraction of the data measured throughout the whole BZ and in multiple zones. Here we will focus only on the α - and β -sheets which are readily identified in the data. The more complex FS pieces will be analyzed and discussed in a separate publication⁴⁴. For CeCoIn_5 these complex pieces display topological differences that depend on whether or not⁴⁵ the FS contains the Ce f -electron, *i.e.*, whether the FS is "large" or "small." For CeCoIn_5 ARPES finds^{28,29} that the Ce 4f electrons behave predominantly localized for the present measurement temperature even though low T de Haas van Alphen experiments^{25–27} unambiguously detect the large FS. For the α and β -sheets discussed here LDA calculations⁴⁵ performed for isoelectronic CeRhIn_5 with the Ce f -electron confined to the core show only small changes in size and no dramatic topological changes due to localizing the f -electron and excluding it from the FS. Nonetheless we will now see that these sheets display large size changes as x varies from 0 to 1. For $x = 0$ and 1 these size changes are in good agreement with findings from dHvA experiments³⁰ and accompanying LDA calculations for YbCoIn_5 . However for the intermediate value of x there is an important difference from the dHvA results, as discussed below.

The two mesh models at the top right and left in the figure show for $x = 0$ the three dimensional shapes of the α -sheet and the β -sheet, respectively. The mesh models are based on an itinerant LDA calculation and are taken from Ref. 46. The α -sheet is a nearly two-dimensional infinite cylinder along the (001)-direction (k_z -direction). Measurements using the de Haas van Alphen effect observe three distinct (001) frequencies which LDA identifies as not only the Γ -plane diamond (α_2) and Z-plane square (α_3) orbits but also a slightly larger circular orbit (α_1) just above and below the Z-plane²⁵. Comparing the mesh models with the ARPES measurements, we identify the large round contours centered on the BZ corners as coming from the quasi-two-dimensional α -sheet. Consistent with this identification, this contour evolves from a diamond-like shape in the Γ -plane of CeCoIn_5 to a slightly squarish shape in the Z-plane. Due to the experimental broadening of ARPES in the k_z -direction, the observed Z-plane α -sheet contour has a distinctly broader width with a squarish inside edge and a rounder outside edge, which is interpretable as the contour of α_3 being blurred with that of α_1 . For YbCoIn_5 , we can similarly identify the same shapes as belonging to the α -sheet. The contours observed in the Z-plane have more of a squarish shape than those of CeCoIn_5 , perhaps con-

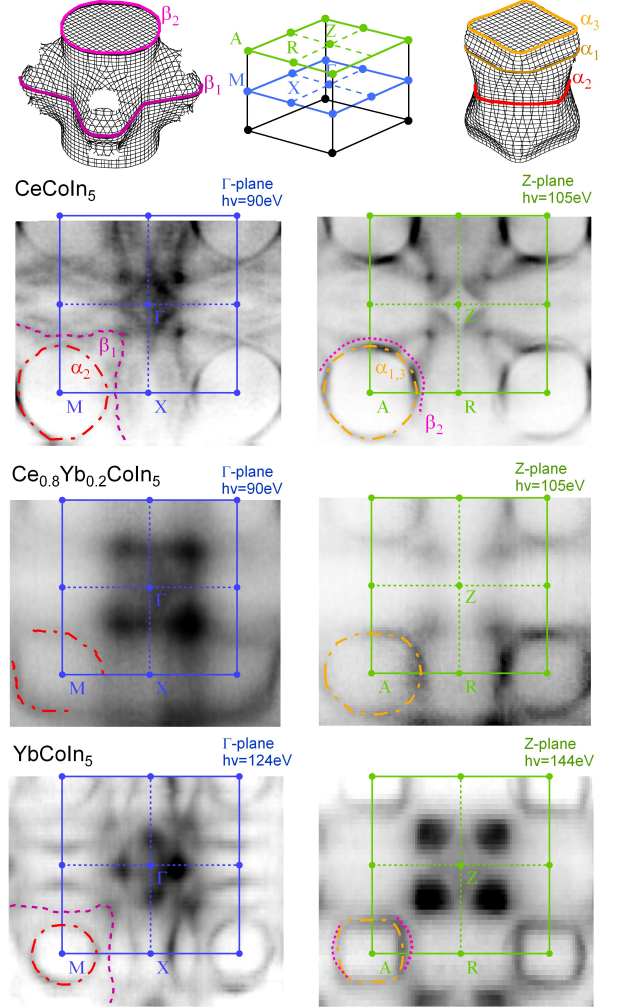


FIG. 7: Second, third and fourth rows show Fermi-surface maps for the Γ and Z planes for $x = 0, 0.2$ and 1 at 26 K, 26 K and 20 K respectively. Top row figures at right and left show respectively mesh models⁴⁶ of the columnar α and β -sheets as calculated in LDA, and middle figure shows the Brillouin zone and measurement planes. The change of size of the α and β -sheets is easily seen.

sistent with LDA calculations³⁰ for YbCoIn_5 that show a somewhat different α column shape. The LDA calculations also show corrugations for intermediate k -values that can give rise to two other orbits likely seen in dHvA but not resolved in ARPES. We next identify the β -sheet as the flower-like lobes in the Γ -planes of CeCoIn_5 and YbCoIn_5 . Although the circular shape of the β -sheet is harder to observe in the Z-plane, we note small crescent-like pieces which are clearly visible aligned along the AR-direction. The low intensity of the β -sheets along the AZ-direction is most likely caused by a matrix element selection rule. For $x = 0.2$ the data allow only an identification of the α sheet cross-sections but not those of the β sheet.

| Composition | ARPES | | | | dHvA | | |
|-------------|----------------|-------------------------------------|------------------------|-------------------|---|---------------------------------|---|
| | Label | FS-Area (π/a) ² | FS Area rel. to x=0 | $\Delta\nu$ kT | Ref. 30 $\Delta\nu$ kT | Ref. 26 $\Delta\nu$ kT | Ref. 25 $\Delta\nu$ kT |
| x=0 | $\alpha_{1,3}$ | 0.85 ± 0.06 | 1 | 4.1 ± 0.3 | 5.46 (α_1)/4.37 (α_3) | 5.401 (F_5)/4.566 (F_3) | 5.56 (α_1)/4.24 (α_3) |
| | α_2 | 0.81 ± 0.06 | 1 | 3.9 ± 0.3 | 4.87 (α_2) | 5.161 (F_4) | 4.53 (α_2) |
| | β_1 | 1.8 ± 0.15 | 1 | 8.7 ± 0.7 | 11.6 (β_1) [†] | | 12.0 (β_1) |
| | β_2 | 1.12 ± 0.15 | 1 | 5.4 ± 0.7 | 7.4 (β_2) [†] | 7.535 (F_6) | 7.5 (β_2) |
| x=0.2 | α_1 | 0.77 ± 0.15 | 0.91 | 3.7 ± 0.7 | | | |
| | α_2 | 0.74 ± 0.2 | 0.91 | 3.6 ± 1 | | | |
| x=1 | α_1 | 0.46 ± 0.08 | 0.54 | 2.2 ± 0.4 | 2.2 (F_5) [†] | | |
| | α_2 | 0.38 ± 0.06 | 0.46 | 1.8 ± 0.3 | 1.6 (F_3) [†] | | |
| | β_1 | 1.1 ± 0.08 | 0.61 | 5.3 ± 0.4 | 6.84 (β_2/F_9) | | |
| | β_2 | 0.5 ± 0.1 | 0.44 | 2.4 ± 0.5 | 3.66 (β_1/F_8) | | |

TABLE I: Left portion: Fermi-surface cross-sectional areas and implied dHvA frequencies from ARPES Fermi-surface maps calculated in units of kilo Tesla (kT); Right portion: Measured dHvA frequencies with original paper labeling shown in parentheses. For $x = 1$ Ref. 30 reverses the labeling of the β -sheet orbits from that used for $x = 0$ such that β_1 corresponds to the Z-plane and β_2 corresponds to the Γ -plane. [†]Value extracted from a publication graph because not explicitly tabulated.

Comparing $x = 0$ to 0.2 to 1, the noteworthy change clearly visible by eye in the FS maps is the considerable reduction of size for the α -sheet and the β -sheet. In contrast to the conclusion of Ref. 16, our results show that the electronic structure along the Γ -M line is much different for $x = 0$ and $x = 1$, even though the general shapes of the α and β -sheets are much the same. We have made a quantitative analysis to determine the cross-section areas in units of $(\pi/a)^2$, along with the implied dHvA frequencies. The results are listed in Table II along with measured dHvA frequencies for $x = 0$ and 1. As discussed below a direct comparison to dHvA frequencies for $x = 0.2$ is not possible. For $x = 0$ there is good general agreement among the dHvA frequencies for the three studies cited. The ARPES frequencies have a similar pattern of variation in magnitude among the various orbits but are systematically smaller than those from dHvA, a difference for which one can consider two contributing effects. The first is the difference in temperature of the two measurements, that low- T dHvA sees the "large" FS and that higher- T ARPES likely sees the "small" FS or at least a smaller FS. However dHvA²⁵⁻²⁷ and LDA⁴⁵ studies find that the fractional differences occurring in the α and β sheets for the change from localized to itinerant Ce f electrons in the Ce 115 compounds are relatively small, so this effect may not be very important. Second, even at the ARPES measurement temperature the bands are still heavy enough very near E_F over the energy window of the FS maps that the k_F value for an electron pocket is likely to be underestimated. For $x = 1$ neither of these differences are important because the measurement temperatures for dHvA and ARPES are both much less than the characteristic temperature and the bands are light. Indeed here we find much better quantitative agreement between the two techniques. It should however be noted that for the α -sheet the good agreement is aided by assigning the measured dHvA frequencies somewhat differ-

ently than in Ref. 30. In that paper the four frequencies labeled F_3 through F_6 (1.8 kT, 2.04 kT, 2.19 kT and 2.96 kT, respectively) are all associated with the α -sheet but F_4 is assigned to α_1 and F_6 is assigned to α_2 , leaving F_3 and F_5 to be assigned to the corrugations predicted in LDA between the Γ -plane and the Z-plane. Considering the shape of the LDA α -sheet we find it more natural and in better agreement with ARPES to assign F_4 as α_1 and F_6 as α_2 , with the other two belonging to the corrugations. These reassignments are not inconsistent with the observed angular dependences of the orbits.

Table II also lists values for the ARPES FS areas for $x = 1$ and $x = 0.2$ relative to those for $x = 0$. For the Γ -plane, the ratio between the α -sheet area in YbCoIn₅ compared to the area in CeCoIn₅ is 0.46, while for the Z-plane this ratio is 0.54. From these data we would estimate that the average ratio of the volumes of the α -sheets is roughly 50%. We note that Ref. 30 also concluded a value of about 50% from the dHvA data, but the combination of the larger dHvA frequencies for $x = 0$ and our changed orbit assignments for $x = 1$, as discussed in the preceding paragraph, causes the dHvA data of Table II to imply a ratio somewhat smaller, perhaps 40%. The ratio of the volumes of the β -sheets is estimated to be about 50% from the ARPES and dHvA data. By the electron counting discussion in Section IB, one would expect for ARPES the total FS volume of YbCoIn₅ compared to that of CeCoIn₅ to include 2 electrons/Yb compared to 3 electrons/Ce which results in a ratio of 66%, whereas for dHvA the FS volume would change from including 2 electrons/Yb to 4 electrons/Ce which results in a ratio of 50%. Considering the uncertainties discussed in the preceding paragraph, and that we can not expect any particular part of the FS to change in strict proportion to the change of the total, these findings are very consistent with the general expectations of simple electron counting.

The significant finding for the ARPES data for $x = 0.2$ is that the α -sheet areas are, even by eye, intermediate between those for $x = 0$ and $x = 1$. Quantitatively the change in area from $x = 0$ to $x = 0.2$ is 21% and 14% of the change from $x = 0$ to $x = 1$ for α_1 and α_2 respectively, i.e. roughly in the same proportion as the doping. Unfortunately it is not possible to compare this result with the dHvA data for intermediate values of x . Although the frequency F_7 of the dHvA data is very similar to that implied by the ARPES data (i.e. 3.6 kT or 3.7 kT) this association cannot be made because F_7 has hardly any variation with x and in Ref. 30 is thought to be associated somehow with the β -sheet. Indeed the dHvA frequencies associated with the α -sheets and β -sheets of the end members $x = 0$ and $x = 1$ show only slight modification for intermediate x -values, quite different from the ARPES finding here of a clear intermediate α -sheet size for an intermediate x -value. We have no hypothesis for this very great difference beyond the possibility of some sample difference for intermediate x .

VI. SUMMARY AND CONCLUSIONS

There are three main new findings of this work for $\text{Ce}_{1-x}\text{Yb}_x\text{CoIn}_5$. First, for small values of x increasing from 0, the Yb valence changes rapidly from being nearly trivalent to the value of 2.3 found previously for larger x and for YbCoIn_5 . Second, we have directly observed a large reduction in the sizes of the columnar α and β FS features for $x = 1$ relative to those for $x = 0$. As already noted, both of these findings are in very good agreement with dHvA results³⁰. Taken together, these results imply that around $x = 0.2$ a change of Yb valence drives a switch of the near E_F electronic structure from one characteristic of $x = 0$ with some very heavy mass FS pieces to one characteristic of $x = 1$ with Yb valence around 2.3, a very large Yb T_K and small measured masses. Third, for at least one intermediate x -value and one sheet (α), the FS has been found to evolve between that of the two end members. This third result contrasts quite sharply with the dHvA results, in which the observed frequencies and masses do not evolve significantly with x and change quickly from one to the other, with a mix of both being seen for $x = 0.2$.

What are the implications of these findings for understanding the transport properties? Regarding the two hypotheses mentioned in Section IA, that of cooperative valence fluctuations or coexisting networks of CeCoIn_5 and YbCoIn_5 , the ARPES results clearly favor the former, at least for the samples used in this study. The addition of only a small amount of Yb drives an overall change in the FS and near E_F electronic structure, and there appear to be unified electronic structures presumably involving the f-states of both Ce and Yb. On the other hand the dHvA results lead to a different conclusion. The finding there of aspects of both electronic structures at $x = 0.2$ suggests some coexistence. Further

it is very puzzling that the observed dHvA frequencies, e.g., for the α orbits, do not change as x increases beyond 0.2, given that the FS size changes appear to be driven by simple electron counting and that the total number of electrons to be contained in the FS per rare earth atom certainly changes steadily. Also, as noted in Ref. 30, the switch to a FS with only low mass measured features is inconsistent with the finding that the specific heat is roughly constant with x . This issue gave rise to the conclusion³⁰ that there must be heavy FS pieces for larger x not yet observed in dHvA, possibly the heavier β orbits that were not observed for $x = 0.2$ and 0.55. The change in transport properties across the crystallographically two-phase region between $x = 0.8$ and $x = 1$ also bears thought. The absence of Kondo-like features in the resistivity for $x = 1$ is readily understandable from the Yb valence of 2.3, the implied large T_K and the low dHvA masses. But the presence of these features for $x = 0.8$, very similar to those for $x = 0$, plus the lack of any Yb valence change across the region, implies that the resistivity is due only to the Ce and that the change is simply the result of removing all the Ce from the lattice. In this respect the Ce would seem to be acting independently of the Yb.

What is the role of the Ce and Yb for the SC? That T_c decreases only slowly and gradually with x implies a gradual steady change of some essential ingredients for the SC and it is again tempting to think of Ce and Yb as acting independently. One possibility is that Ce brings a local moment which is essential for the SC. In this picture the smallness of the Ce T_K is a benefit, and Yb, with the largeness of its T_K does no direct harm but does serve to dilute the Ce. Another model involving Ce as the essential active ingredient perhaps being diluted by Yb is the composite pairing picture⁴⁷. Moving away from local pictures, if low dimensionality is involved in the SC, as has been suggested for pairing involving spin fluctuations, then the particulars of the columnar pieces of FS might be important. The changing sizes of these pieces with x in the ARPES data (but not the dHvA data) would be consistent with this idea.

In conclusion, while good progress has been made in determining the electronic structure of this interesting new alloy series, it remains to find a unified view that explains both what is now known about the electronic properties and what is known about the transport properties. One step forward for the future would be to obtain a complete set of ARPES data for intermediate values of x , ideally having the same high quality as that reported here for $x = 0$ and $x = 1$.

VII. ACKNOWLEDGEMENT

Supported by the U.S. DOE at the ALS, Contract No. DE-AC02-05CH11231, at UM, Contract No. DE-FG02-07ER46379 for current work, and at UCSD, Contract No. DE FG02-04ER-46105; by the U.S. NSF at UM, Grant

No. DMR-03-02825 for initial work. The experimental support at ALS beamline 7.0 by E. Rotenberg is gratefully acknowledged. For the EDX measured at the EMAL at the UM, we thank J. Mansfield for discussion and ac-

knowledge the support of NSF grant DMR-0320740. MJ acknowledges support by the Alexander von Humboldt foundation. We thank Sooyoung Jang for assistance in the preparation of Fig. 6.

- ¹ M. B. Maple, R. E. Baumbach, N. P. Butch, J. J. Hamlin, and M. Janoschek, *J. Low Temp. Phys.* **161**, 4 (2010).
- ² P. Coleman, "Heavy Fermions: electrons at the edge of magnetism", chapter in the "Handbook of Magnetism and Advanced Magnetic Materials", edited by H. Kronmüller and S. Parkin, John Wiley & Son, Ltd (2007).
- ³ J. Kondo, *Prog. Theor. Phys.* **32**, 37 (1964).
- ⁴ S. Doniach, *Physica B* **91**, 231 (1977).
- ⁵ Z. Fisk, H. R. Ott, T. M. Rice and J. L. Smith, *Nature* **320**, 124 (1986).
- ⁶ C. Pfleiderer, *Rev. Mod. Phys.* **81**, 1551 (2009).
- ⁷ N. D. Mathur, F. M. Grosche, S. R. Julian, I. R. Walker, D. M. Freye, R. K. W. Haselwimmer, G. G. Lonzarich, and W. Gilbert, *Nature* **394**, 39 (1998).
- ⁸ C. Petrovic, P. G. Pagliuso, M. F. Hundley, R. Movshovich, J. L. Sarrao, J. D. Thompson, Z. Fisk, and P. Monthoux, *J. Phys.: Condens. Matter* **13**, L337 (2001).
- ⁹ V. A. Sidorov, M. Nicklas, P. G. Pagliuso, J. L. Sarrao, Y. Bang, A. V. Balatsky, and J. D. Thompson, *Phys. Rev. Lett.* **89**, 157004 (2002).
- ¹⁰ C. Stock, C. Broholm, J. Hudis, H.J. Kang, and C. Petrovic, *Phys. Rev. Lett.* **100**, 087001 (2008).
- ¹¹ S. Nakatsuji, D. Pines and Z. Fisk, *Phys. Rev. Lett.* **92**, 016401 (2004).
- ¹² J. Paglione, T. A. Sayles, P.-C. Ho, J. R. Jeffries, and M. B. Maple, *Nature Physics* **3**, 703 (2007).
- ¹³ E. D. Bauer, Y.-F. Yang, C. Capan, R. R. Urbano, C. F. Miclea, H. Sakai, F. Ronning, M. J. Graf, A. V. Balatsky, R. Movshovich, A. D. Bianchi, A. P. Reyes, P. L. Kuhns, J. D. Thompson, and Z. Fisk, *Proc. Natl. Acad. Sci. (USA)* **108**, 6857 (2011).
- ¹⁴ C. Capan, G. Seyfarth, D. Hurt, B. Prevost, S. Roorda, A. D. Bianchi and Z. Fisk, *Europhys. Lett.* **92**, 47004 (2010).
- ¹⁵ L. Shu, R. E. Baumbach, M. Janoschek, E. Gonzales, K. Huang, T. A. Sayles, J. Paglione, J. O'Brien, J. J. Hamlin, D. A. Zocco, P.-C. Ho, C. A. McElroy, and M. B. Maple, *Phys. Rev. Lett.* **106**, 156403 (2011).
- ¹⁶ C. H. Booth, T. Durakiewicz, C. Capan, D. Hurt, A. D. Bianchi, J. J. Joyce, and Z. Fisk, *Phys. Rev. B* **83**, 235117 (2011).
- ¹⁷ Y.-F. Yang, Z. Fisk, H.-O. Lee, J. D. Thompson, and D. Pines, *Nature* **454**, 611 (2008).
- ¹⁸ Y. Mizukami, H. Shishido, T. Shibauchi, M. Shimozawa, S. Yasumoto, D. Watanabe, M. Yamashita, H. Ikeda, T. Terashima, H. Kontani, and Y. Matsuda, *Nature Physics* **7**, 849 (2011).
- ¹⁹ M. Shimozawa, T. Watashige, S. Yasumoto, Y. Mizukami, M. Nakamura, H. Shishido, S. K. Goh, T. Terashima, T. Shibauchi and Y. Matsuda, *Phys. Rev. B* **86**, 144526 (2012).
- ²⁰ S. Watanabe and K. Miyake, *J. Phys. Soc. Jpn.* **79**, 033707, (2010).
- ²¹ H. Q. Yuan, F. M. Grosche, M. Deppe, C. Geibel, G. Sparn, and F. Steglich, *Science* **302**, 2104, (2003).
- ²² T. Park, V. A. Sidorov, F. Ronning, J. -X. Zhu, Y. Tokiwa, H. Lee, E. D. Bauer, R. Movshovich, J. L. Sarrao, and J. D. Thompson, *Nature* **456**, 366 (2008).
- ²³ T. Park, H. Lee, I. Martin, X. Lu, V. A. Sidorov, K. Gofryk, F. Ronning, E. D. Bauer, and J. D. Thompson, *Phys. Rev. Lett.* **108**, 077003 (2012).
- ²⁴ M. Dzero and X. Huang, *J. Phys: Condens. Matter* **24**, 075603 (2012).
- ²⁵ R. Settai, H. Shishido, S. Ikeda, Y. Murakawa, M. Nakashima, D. Aoki, Y. Haga, H. Harima, and Y. Onuki, *J. Phys. Condens. Mat.* **13**, L627 (2001).
- ²⁶ D. Hall, E. C. Palm, T. P. Murphy, S. W. Tozer, Z. Fisk, U. Alver, R. B. Goodrich, J. L. Sarrao, P. G. Pagliuso, and T. Ebihara, *Phys. Rev. B* **64**, 212508 (2001).
- ²⁷ H. Shishido, R. Settai, D. Aoki, S. Ikeda, R. Nakawaki, N. Nakamura, T. Iizuka, Y. Inada, K. Sugiyama, T. Takeuchi, K. Kindo, T. C. Kobayashi, Y. Haga, H. Harima, Y. Aoki, T. Namiki, H. Sato, and Y. Onuki, *J. Phys. Soc. Jpn.* **71**, 162 (2002).
- ²⁸ J.D. Denlinger, unpublished data.
- ²⁹ A. Koitzsch, I. Opahle, S. Elgazzar, S. V. Borisenko, J. Geck, V. B. Zabolotnyy, D. Inosov, H. Shiozawa, M. Richter, M. Knupfer, J. Fink, B. Büchner, E. D. Bauer, J. L. Sarrao, and R. Follath, *Phys. Rev. B* **79**, 075104 (2009).
- ³⁰ A. Polyakov, O. Ignatchik, B. Bergk, K. Götze, A. D. Bianchi, S. Blackburn, B. Prévost, G. Seyfarth, M. Côte, D. Hurt, C. Capan, Z. Fisk, R. G. Goodrich, I. Sheikin, M. Richter, and J. Wosnitzer, *Phys. Rev. B* **85**, 245119 (2012).
- ³¹ S. Elgazzar, I. Opahle, R. Hayn, and P.M. Oppeneer, *Phys. Rev. B* **69**, 214510 (2004).
- ³² V. S. Zapf, E. J. Freeman, E. D. Bauer, J. Petricka, C. Sirvent, N. A. Frederick, R. P. Dickey, and M. B. Maple, *Phys. Rev. B* **65**, 014506 (2001).
- ³³ C. Petrovic, R. Movshovich, M. Jaime, P.G. Pagliuso, M.F. Hundley, J. L. Sarrao, Z. Fisk, J. D. Thompson, *Europhys. Lett.* **53**, 354 (2001).
- ³⁴ F.J. Himpsel, *Adv. Phys.* **32**, 1 (1983).
- ³⁵ B. T. Thole, G. van der Laan, J. C. Fuggle, G. A. Sawatzky, R. C. Karnatak and J.-M. Esteve, *Phys. Rev. B* **32**, 5107 (1985).
- ³⁶ O. Gunnarsson and K. Schönhammer, *Phys. Rev. B* **28**, 4315 (1983).
- ³⁷ J. C. Fuggle, F. U. Hillebrecht, Z. Zolnieriek, R. Lässer, C. Freiburg, O. Gunnarsson, and K. Schönhammer, *Phys. Rev. B* **27**, 7330 (1983).
- ³⁸ C. Dallera, M. Grioni, A. Palenzona, M. Taguchi, E. Annese, G. Ghiringhelli, A. Tagliaferri, N. B. Brookes, Th. Neisius, and L. Braicovich, *Phys. Rev. B* **70**, 085112 (2004).
- ³⁹ T. Willers, Z. Hu, N. Hollmann, P. O. Körner, J. Gegner, T. Burnus, H. Fujiwara, A. Tanaka, D. Schmitz, H. H. Hsieh, H.-J. Lin, C. T. Chen, E. D. Bauer, J. L. Sarrao, E. Goremychkin, M. Koza, L. H. Tjeng, and A. Severing, *Phys. Rev. B* **81**, 195114 (2010).
- ⁴⁰ F. Gerken, *J. Phys. F* **13**, 703 (1983).
- ⁴¹ K. A. Gschneidner, *Rare Earth Alloys* (D. Van Nostrand

- Company, Inc., Princeton, New Jersey, 1961), pp. 7–12.
- ⁴² Vasyi' I. Zaremba, Ute Ch. Rodewald, Rolf-Dieter Hoffmann, Yaroslav M. Kalychak, and Rainer Pttgen, Z. Anorg. Allg. Chem. **629**, 1157 (2003).
- ⁴³ C. M. Varma and V. Heine, Phys. Rev. B **11**, 4763 (1975).
- ⁴⁴ J. D. Denlinger, F. Wang, R. S. Singh, J. W. Allen, K. Rossnagel, P. M. Oppeneer, V. S. Zapf and M. B. Maple, to be published.
- ⁴⁵ P. M. Oppeneer, S. Elgazzar, A. B. Shick, I. Opahle, J. Rusz, and R. Hayn, J. Magn. Magn. Mater. **310**, 1684 (2007).
- ⁴⁶ H. Shishido, T. Ueda, S. Hashimoto, T. Kubo, R. Settai, H. Harima and Y. Onuki, J. Phys.: Condens. Matter **15**, L499 (2003).
- ⁴⁷ R. Flint, A. H. Nevidomskyy and P. Coleman, Phys. Rev. B **84**, 064514 (2011).